Journal of Geophysical Research: Solid Earth

Supporting Information for

Denoising surface waves extracted from ambient noise using three-station interferometry: Methodology and Application to 1-D linear array

Hongrui Qiu[1], Fenglin Niu[1], and Lei Qin[2]

[1]Department of Earth, Environmental and Planetary Sciences, Rice University, Houston, TX, USA
[2]Department of Earth Sciences, University of Southern California, Los Angeles, CA, USA

Contents of this file

Introduction

This supporting information provides additional details that are complementary to the main article.

Text S1.

Determination of the tapering window

In order to select the accurate time window that outlines the surface wave signal (e.g., black dashed lines in Fig. S5d), we first estimate the array-mean phase and group velocity dispersions (e.g., Fig. S5b) by stacking the denoised waveforms (Fig. S5c) shifted with respect to different moveout velocities (Fig. S5a). Figure S5a shows the procedure of grid searching the array-mean phase and group velocities at 0.3 s:

1. For each analyzed moveout velocity V_0 (x-axis of Fig. 5a), we shift the denoised waveform of each station pair with interstation distance of Δ towards the negative correlation time direction with d$t = \Delta/V_0$.
2. We directly stack the denoised waveforms after the alignment and measure the maximum amplitude of the stacked waveform (red dots in Fig. 5a). The array-mean phase velocity is then determined as the velocity V_0 when the grid search curve (red dashed curve in Fig. 5a) reaches the maximum.
3. To estimate the array-mean group velocity, we stack envelope functions of the shifted waveforms. The result for grid search of array-mean group velocity is shown in cyan color.

After obtaining the array-mean phase and group velocities at each period, $\bar{V}_{\mathrm{ph}}$ and $\bar{V}_{\mathrm{gp}}$, we set the width of the tapering window as four times the dominate period $T_{\max}$ of the array-mean amplitude spectrum (e.g., Fig. 4d). The center of the window is set to $N{\cdot}T_{\max}$, where N is a integer that satisfies $N{\cdot}T_{\max} \geq \Delta \cdot \left(1/\bar{V}_{\mathrm{ph}} - 1/\bar{V}_{\mathrm{gp}}\right) > (N-1){\cdot}T_{\max}$, for the station pair with interstation distance of Δ.

Text S2.

Three-station interferometry with the presence of higher-mode surface waves

The aim of this section is to investigate the derivation for denoising using three-station interferometry if higher-mode surface waves are present. For simplicity, we first only add the first overtone surface wave, $\widetilde{M}_{i\_j}(\omega)$, to equation 2b:

$$\begin{aligned}\tilde{G}_{i\_j}(\omega) &= \tilde{S}_{i\_j}(\omega) + \tilde{O}_{i\_j}(\omega) = \tilde{F}_{i\_j}(\omega) + \widetilde{M}_{i\_j}(\omega) + \tilde{O}_{i\_j}(\omega) \\ &= A_{F\_ij} \cdot e^{-i\left(\omega \cdot T_{ij}^{F} + \varphi_F\right)} + A_{M\_ij} \cdot e^{-i\left(\omega \cdot T_{ij}^{M} + \varphi_M\right)} + \tilde{O}_{i\_j}(\omega),\end{aligned} \tag{S1}$$

where T_{ij}^{M} and φ_M are phase travel time and initial phase of the first overtone surface wave, respectively.

By performing three-station interferometry, we plug equation S1 into equation 4a:

$$\tilde{I}_{i\_j}(\omega; k) = \tilde{I}_{i\_j}^{F}(\omega; k) + \tilde{I}_{i\_j}^{M}(\omega; k) + \tilde{I}_{i\_j}^{FM}(\omega; k) + \tilde{I}_{i\_j}^{O}(\omega; k), \tag{S2}$$

where each component is given by:

$$\tilde{I}^{F}_{i\_j}(\omega;k) = A_{F\_ik}\cdot A_{F\_jk}\cdot e^{i\varphi_{ij\_k}} = \begin{cases} \tilde{F}^{*}_{i\_k}(\omega)\cdot\tilde{F}_{j\_k}(\omega), & k<i \\ \tilde{F}_{i\_k}(\omega)\cdot\tilde{F}_{j\_k}(\omega), & i<k<j, \\ \tilde{F}_{i\_k}(\omega)\cdot\tilde{F}^{*}_{j\_k}(\omega), & k>j \end{cases} \quad \text{(S3a)}$$

$$\tilde{I}^{M}_{i\_j}(\omega;k) = \begin{cases} \widetilde{M}^{*}_{i\_k}(\omega)\cdot\widetilde{M}_{j\_k}(\omega), & k<i \\ \widetilde{M}_{i\_k}(\omega)\cdot\widetilde{M}_{j\_k}(\omega), & i<k<j, \\ \widetilde{M}_{i\_k}(\omega)\cdot\widetilde{M}^{*}_{j\_k}(\omega), & k>j \end{cases} \quad \text{(S3b)}$$

$$\tilde{I}^{FM}_{i\_j}(\omega;k) = \begin{cases} \tilde{F}^{*}_{i\_k}(\omega)\cdot\widetilde{M}_{j\_k}(\omega)+\widetilde{M}^{*}_{i\_k}(\omega)\cdot\tilde{F}_{j\_k}(\omega), & k<i \\ \tilde{F}_{i\_k}(\omega)\cdot\widetilde{M}_{j\_k}(\omega)+\widetilde{M}_{i\_k}(\omega)\cdot\tilde{F}_{j\_k}(\omega), & i<k<j, \\ \tilde{F}_{i\_k}(\omega)\cdot\widetilde{M}^{*}_{j\_k}(\omega)+\widetilde{M}_{i\_k}(\omega)\cdot\tilde{F}^{*}_{j\_k}(\omega), & k>j \end{cases} \quad \text{(S3c)}$$

and

$$\tilde{I}^{O}_{i\_j}(\omega;k) = \begin{cases} \tilde{G}^{*}_{i\_k}(\omega)\cdot\tilde{O}_{j\_k}(\omega)+\tilde{O}^{*}_{i\_k}(\omega)\cdot\tilde{S}_{j\_k}(\omega), & k<i \\ \tilde{G}_{i\_k}(\omega)\cdot\tilde{O}_{j\_k}(\omega)+\tilde{O}_{i\_k}(\omega)\cdot\tilde{S}_{j\_k}(\omega), & i<k<j. \\ \tilde{G}_{i\_k}(\omega)\cdot\tilde{O}^{*}_{j\_k}(\omega)+\tilde{O}_{i\_k}(\omega)\cdot\tilde{S}^{*}_{j\_k}(\omega), & k>j \end{cases} \quad \text{(S3d)}$$

Combined with equation 3a, the terms $\tilde{I}^{F}_{i\_j}(\omega;k)$ and $\tilde{I}^{M}_{i\_j}(\omega;k)$ are only related to the fundamental mode and the first overtone surface waves, respectively, and therefore are independent on *k* value in phase as illustrated in equation 4b. On the other hand, the term $\tilde{I}^{O}_{i\_j}(\omega;k)$ is associated with non-surface wave signals $\tilde{O}(\omega)$, and therefore varies significantly with *k* value in phase.

For the term $\tilde{I}^{FM}_{i\_j}(\omega;k)$ that represents the interference between the two modes of surface waves, we can further expand equation S3c by plugging in equation S1:

$$\tilde{I}^{FM}_{i\_j}(\omega;k) = \begin{cases} A_{FM\_k}\cdot e^{-i\omega\cdot\left(T^{F}_{ik}-T^{M}_{jk}\right)}+A_{MF\_k}\cdot e^{-i\omega\cdot\left(T^{M}_{ik}-T^{F}_{jk}\right)}, & k<i \\ A_{FM\_k}\cdot e^{-i\left[\omega\cdot\left(T^{F}_{ik}+T^{M}_{jk}\right)+\varphi_{FM}\right]}+A_{MF\_k}\cdot e^{-i\left[\omega\cdot\left(T^{M}_{ik}+T^{F}_{jk}\right)+\varphi_{FM}\right]}, & i<k<j\cdot \\ A_{FM\_k}\cdot e^{-i\omega\cdot\left(T^{M}_{ik}-T^{F}_{jk}\right)}+A_{MF\_k}\cdot e^{-i\omega\cdot\left(T^{F}_{ik}-T^{M}_{jk}\right)}, & k>j \end{cases} \quad \text{(S4)}$$

where $A_{FM\_k} = A_{F\_ik}\cdot A_{M\_jk}$, $A_{MF\_k} = A_{M\_ik}\cdot A_{F\_jk}$, and $\varphi_{FM} = \varphi_F + \varphi_M$. The travel time differences of $T^{F}_{ik} - T^{M}_{jk}$ and $T^{M}_{ik} - T^{F}_{jk}$ for $k < i$ are dependent on the choice of *k*, and it is also true for cases when $k < j$ and $i < k < j$. Therefore, the terms $\tilde{I}^{FM}_{i\_j}(\omega;k)$ and $\tilde{I}^{O}_{i\_j}(\omega;k)$ are suppressed through the stacking introduced in section 3.2 (Equation 5b). This is equivalent to that, after stacking, only the terms $\tilde{I}^{F}_{i\_j}(\omega;k)$ and $\tilde{I}^{M}_{i\_j}(\omega;k)$ are preserved, i.e., the denoised waveform will only enhance the fundamental mode and first overtone surface waves but suppress the contributions from non-surface wave signals and the interference pattern between the two modes. Similar formulations can easily be derived for cases when more than two modes of surface waves are present.

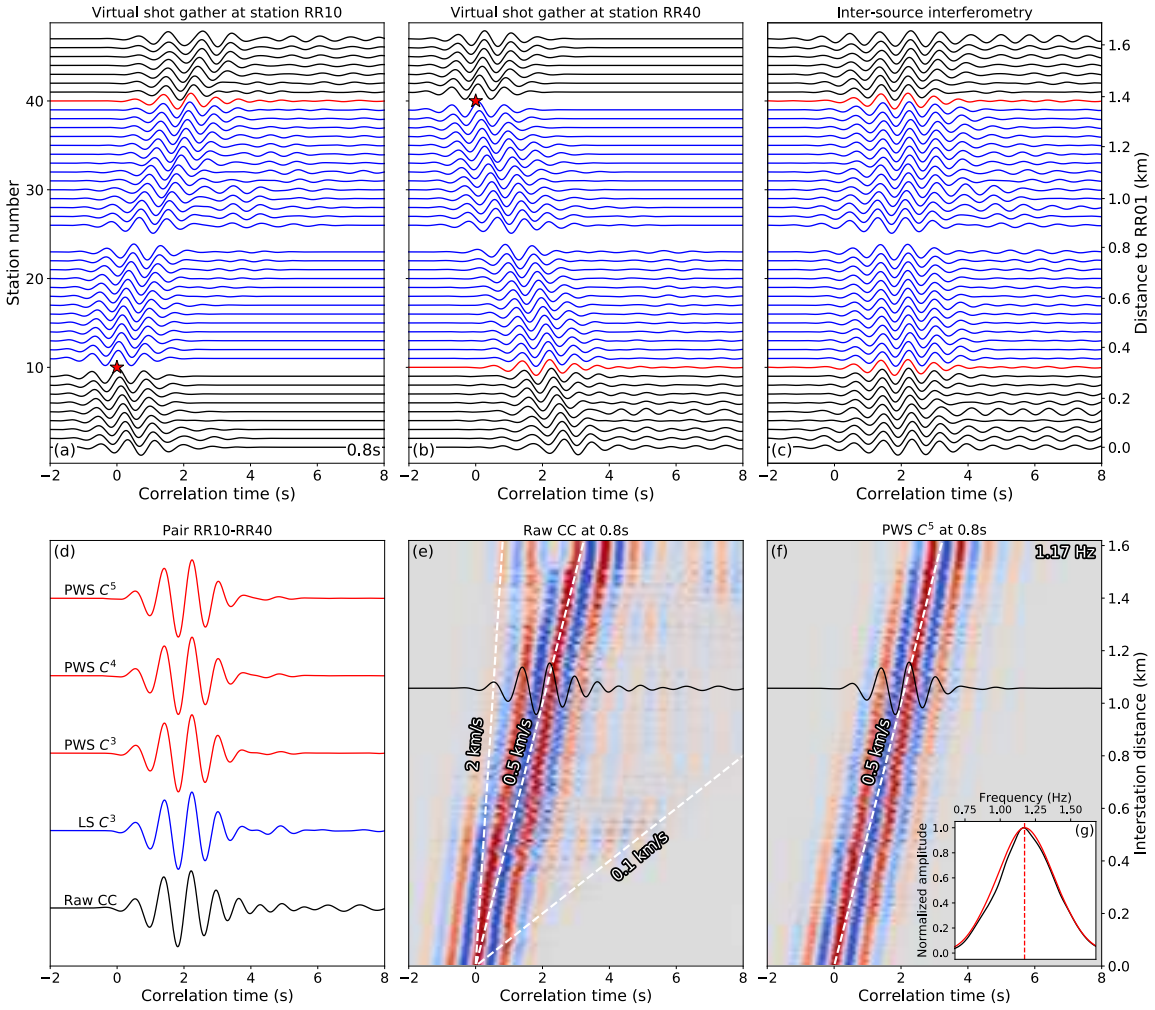

Figure S1. (a)-(c) Same as Fig. 2 for TT component data narrow bandpass filtered at 0.8 s. (d)-(g) Same as Fig. 3 for TT component data narrow bandpass filtered at 0.8 s. Signal to noise ratio of the fundamental mode surface waves is much higher in the filtered ANCs, (a)-(b), than that of Fig. 2. As illustrated in panel (c), the systematic time shift between black and blue waveforms is zero, suggesting φ_F (Equation 2b) is zero. Comparison between panels (e) and (f) suggests that the denoising process mainly suppresses coda waves of the filtered ANCs at low frequency (0.8 s).

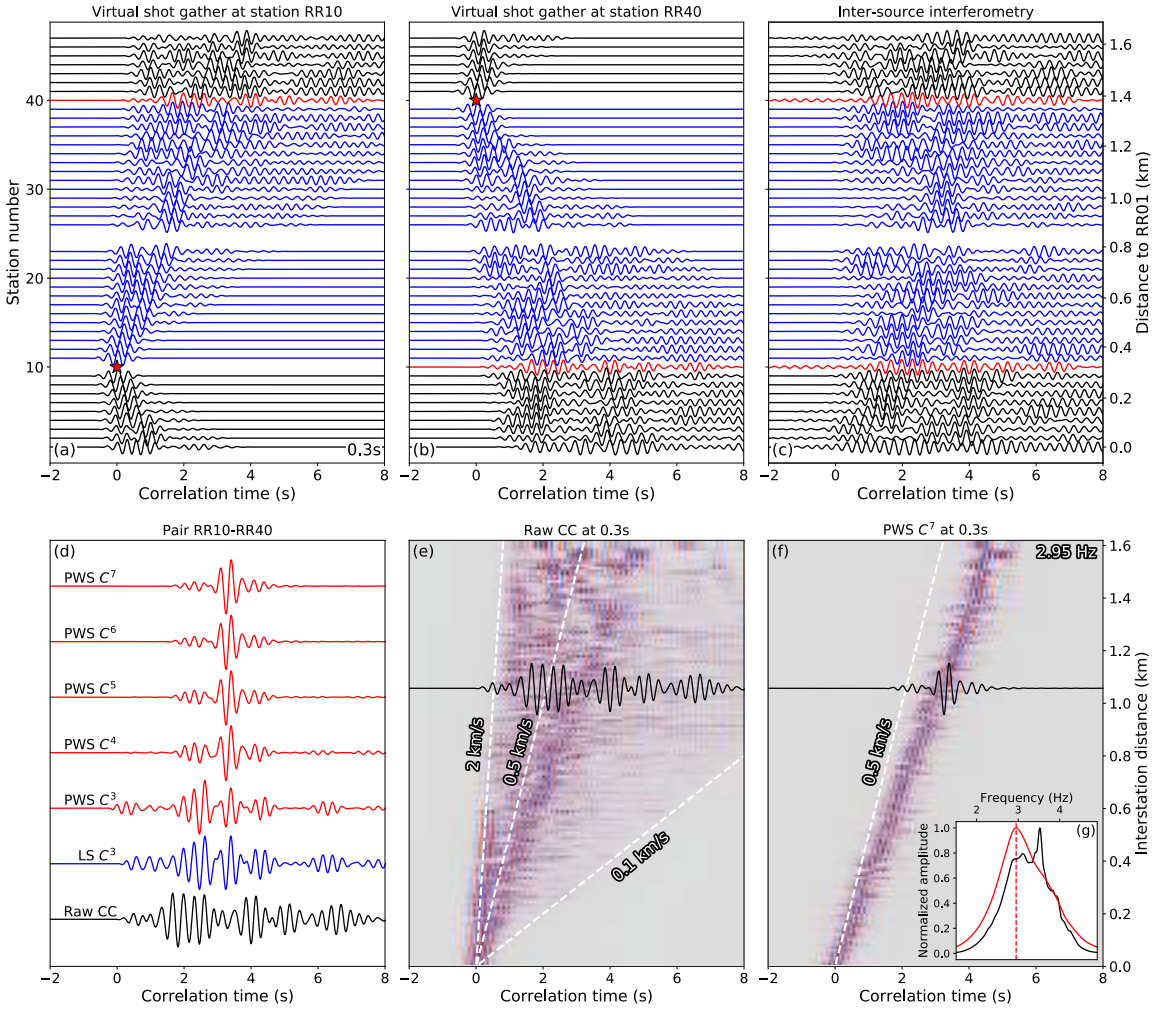

Figure S2. Same as Fig. S1 for ZZ component data narrow bandpass filtered at 0.3 s. Similar to Fig. 3, signal to noise ratio of the fundamental mode surface waves is low.

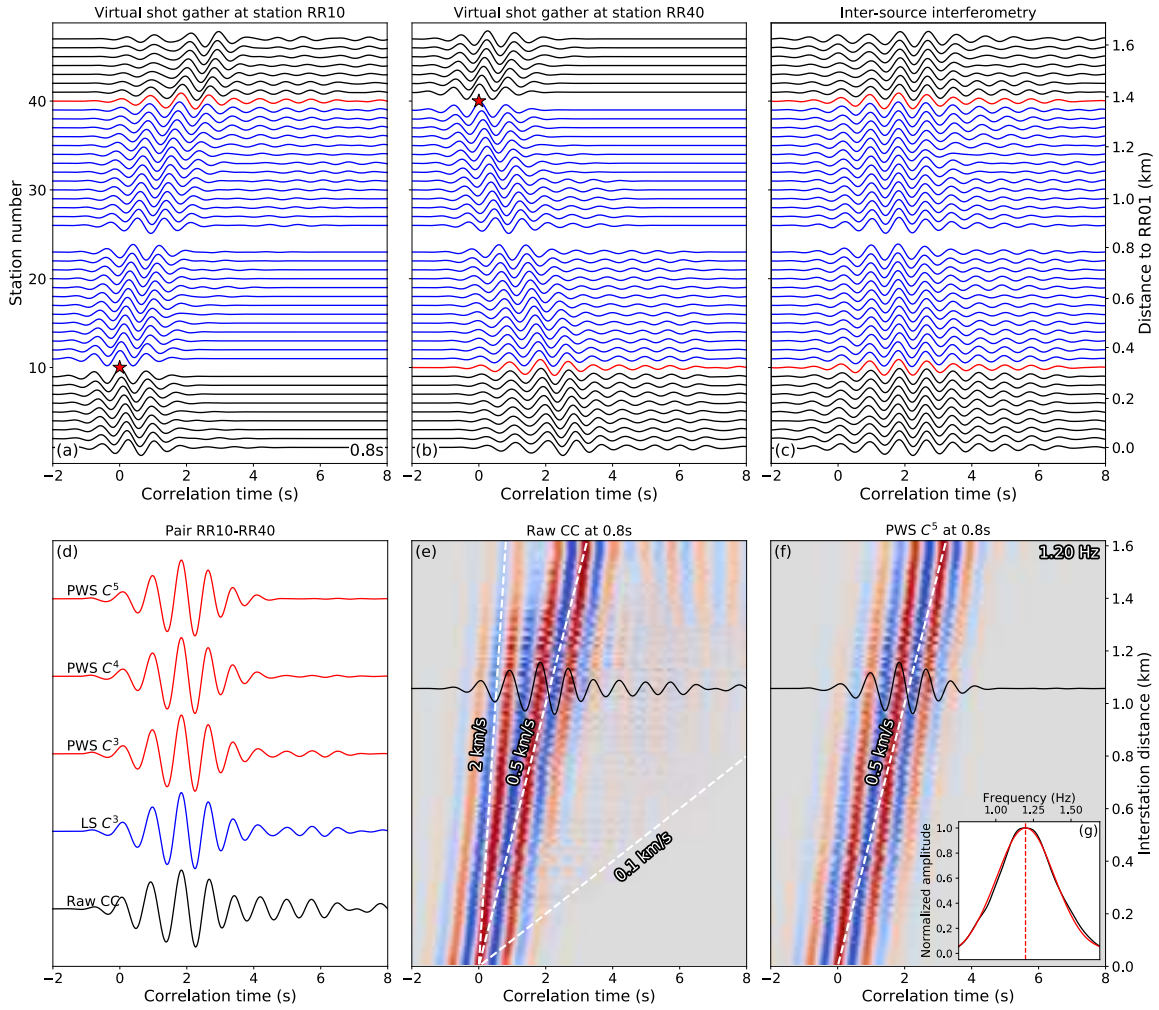

Figure S3. Same as Fig. S2 for the denoising of ZZ component data narrow bandpass filtered at 0.8 s.

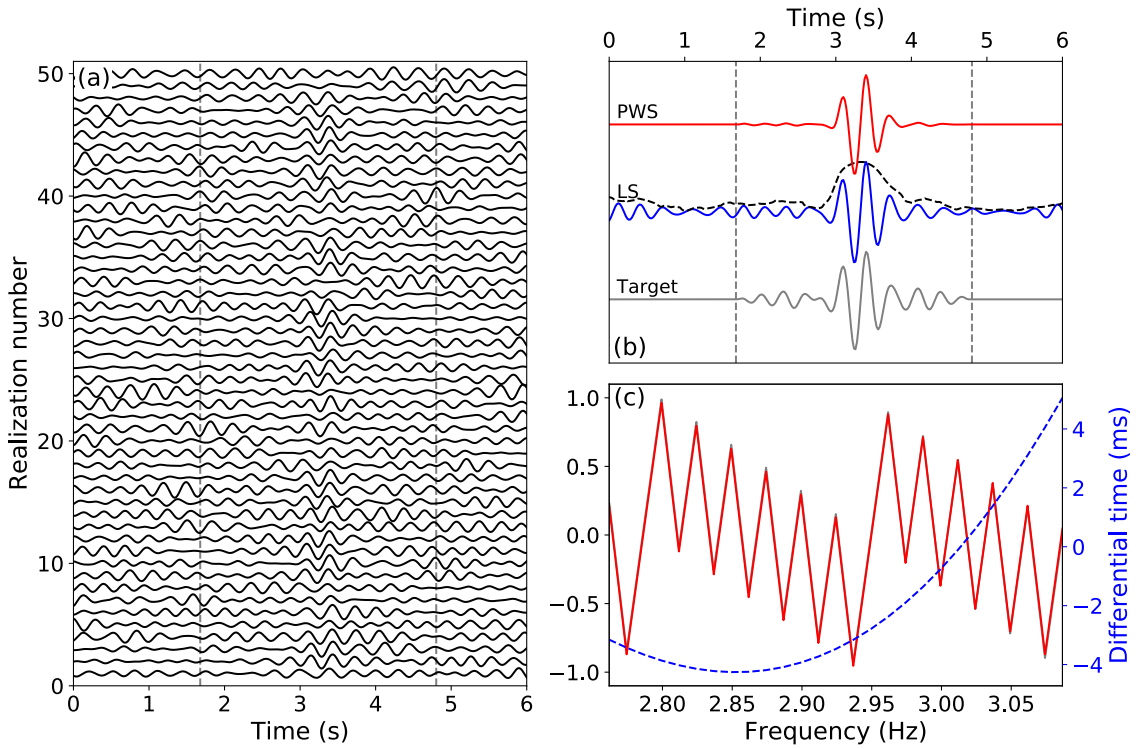

Figure S4. Synthetic test for phase weighted stacking…

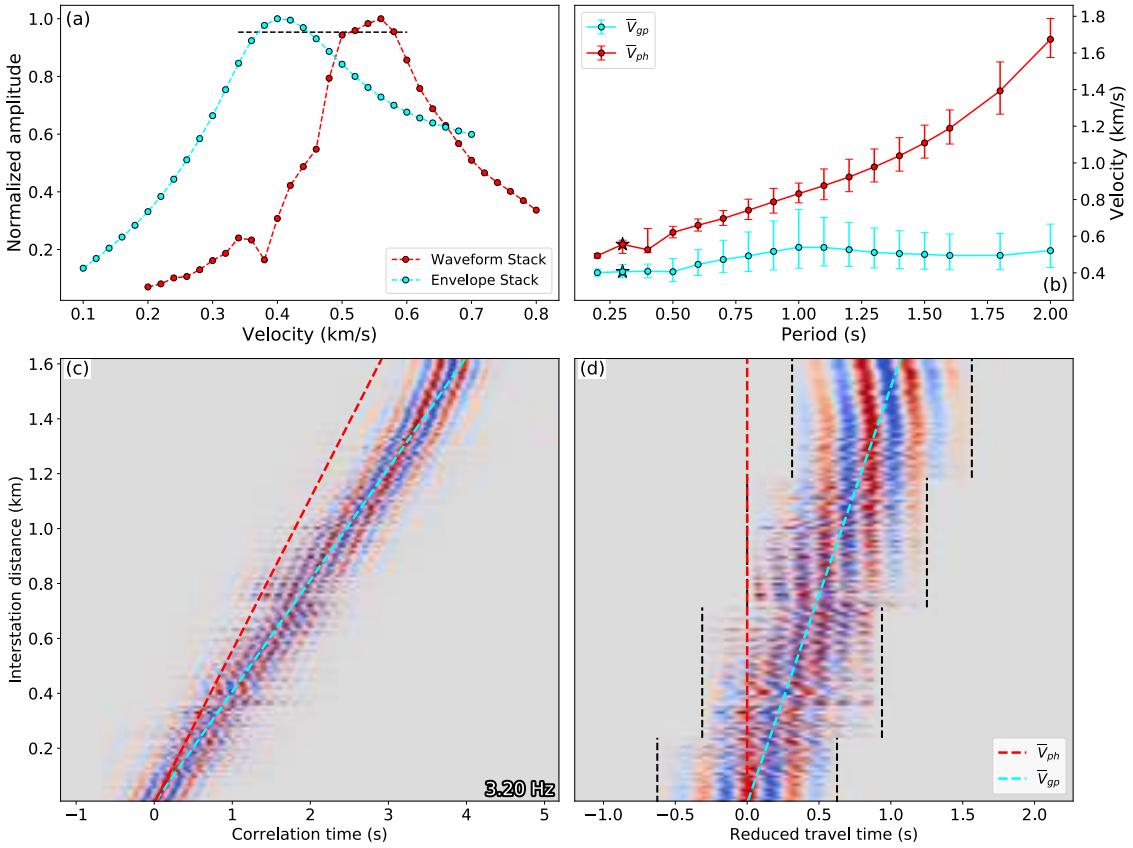

Figure S5. (a) Phase (red) and group (cyan) velocity are estimated as the velocity of the peak of the curve using data at TT component narrow bandpass filtered and denoised at 0.3 s (shown in Fig. 3c), assuming a homogenous velocity structure beneath the array (Appendix I). The black dashed line is used to estimate uncertainty of the array-mean velocity. (b) Array-mean phase (red) and group (cyan) velocity dispersion curves, with error bars indicating the estimated uncertainty. Stars depict the array-mean velocities obtained in (a). (c) Same as Fig. 4c with the red and cyan dashed lines illustrating the moveout of array-mean phase and group velocities. Peak frequency of the array-mean amplitude spectrum (dashed lines in Fig. 4d) is labeled at the bottom right. (d) Waveforms aligned with respect to the travel time predicted by the array-mean phase velocity (red dashed line). The waveforms are further tapered using time windows outlined by the black dashed lines (Appendix I). The cyan dashed line indicates the array-mean group velocity moveout after the alignment.

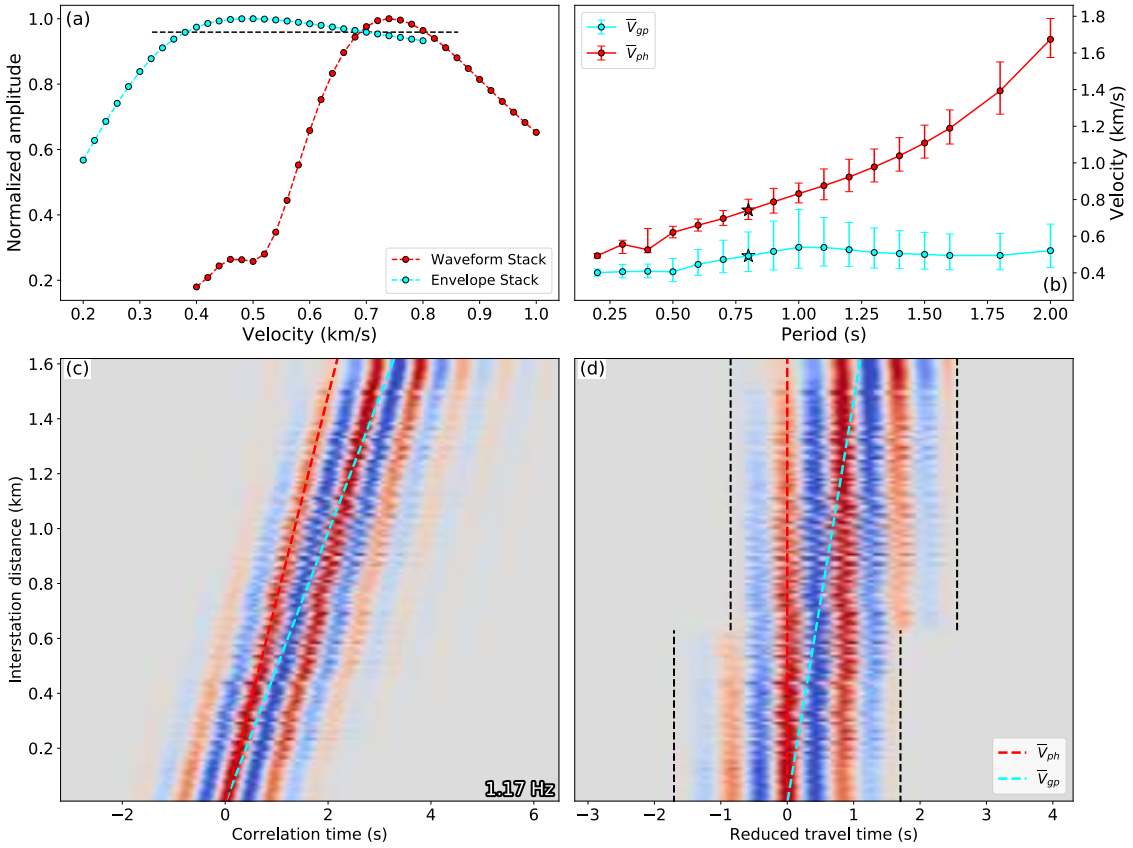

Figure S6. Same as Fig. S5 for TT component data narrow bandpass filtered at 0.8 s.

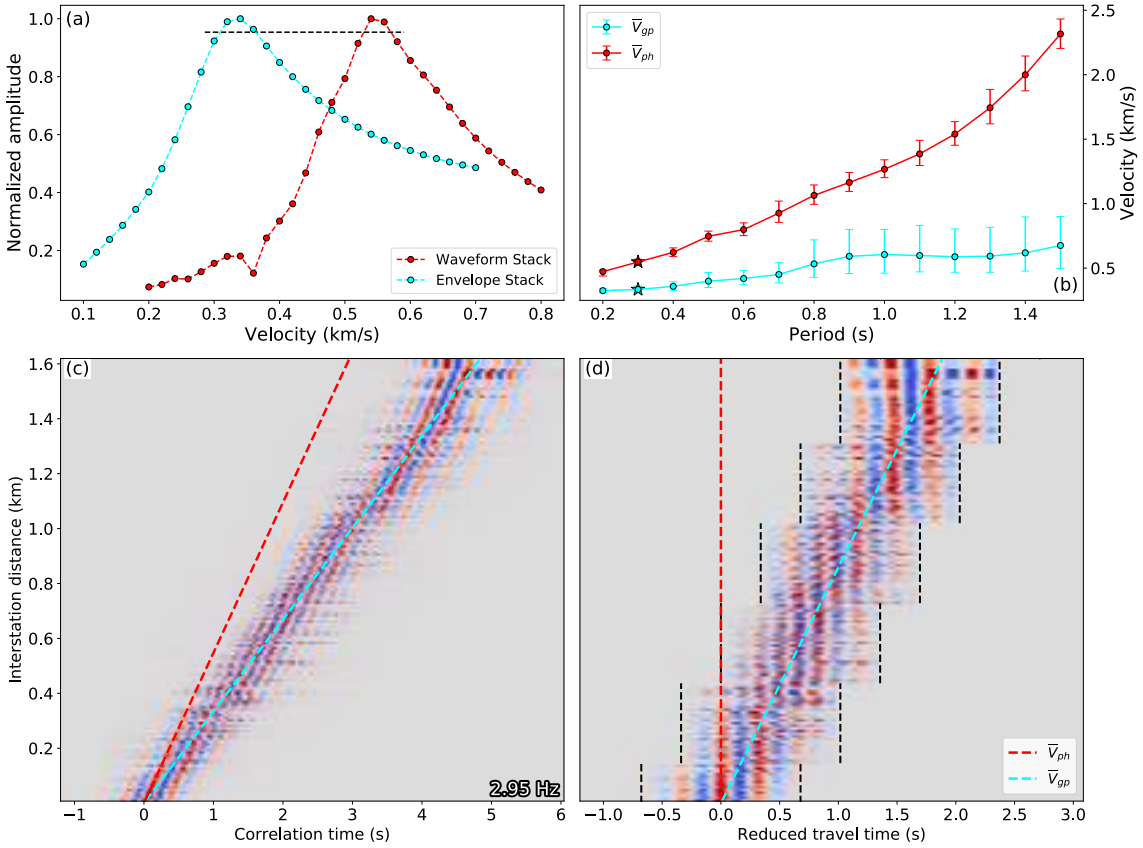

Figure S7. Same as Fig. S5 for ZZ component data narrow bandpass filtered at 0.3 s.

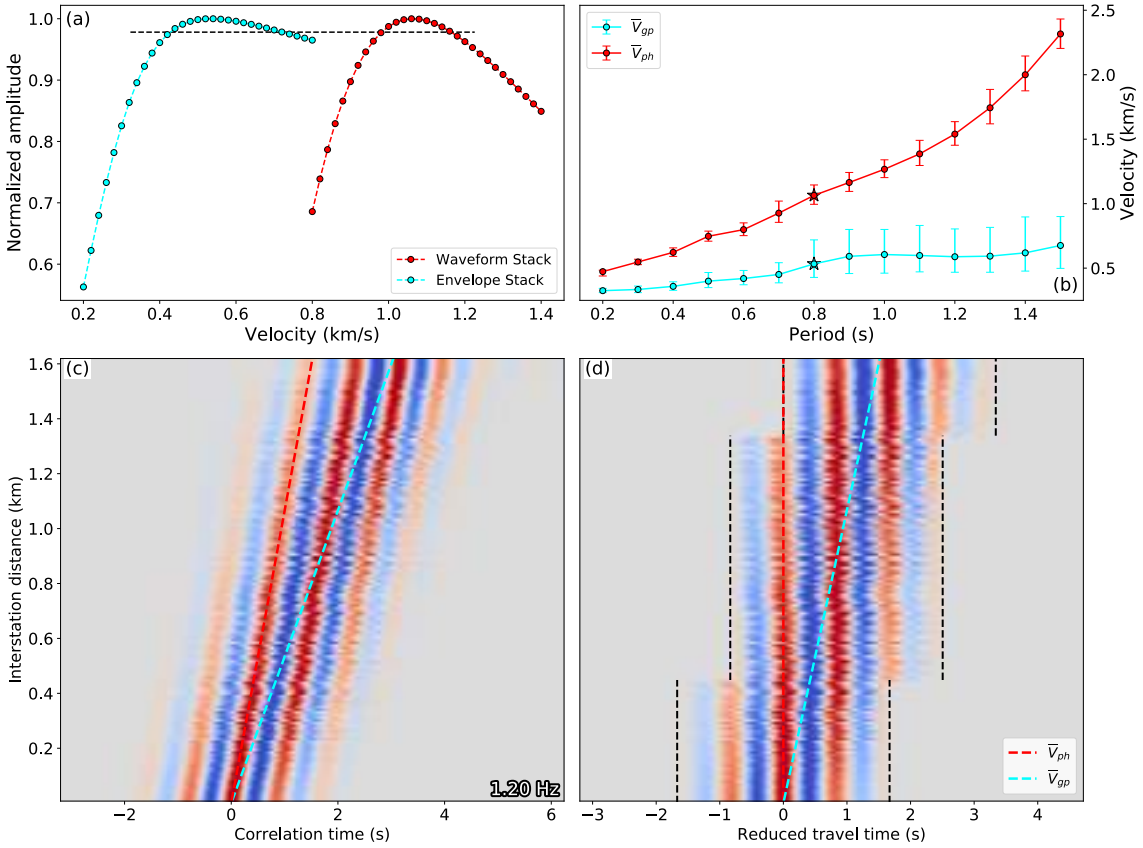

Figure S8. Same as Fig. S5 for ZZ component data narrow bandpass filtered at 0.8 s.

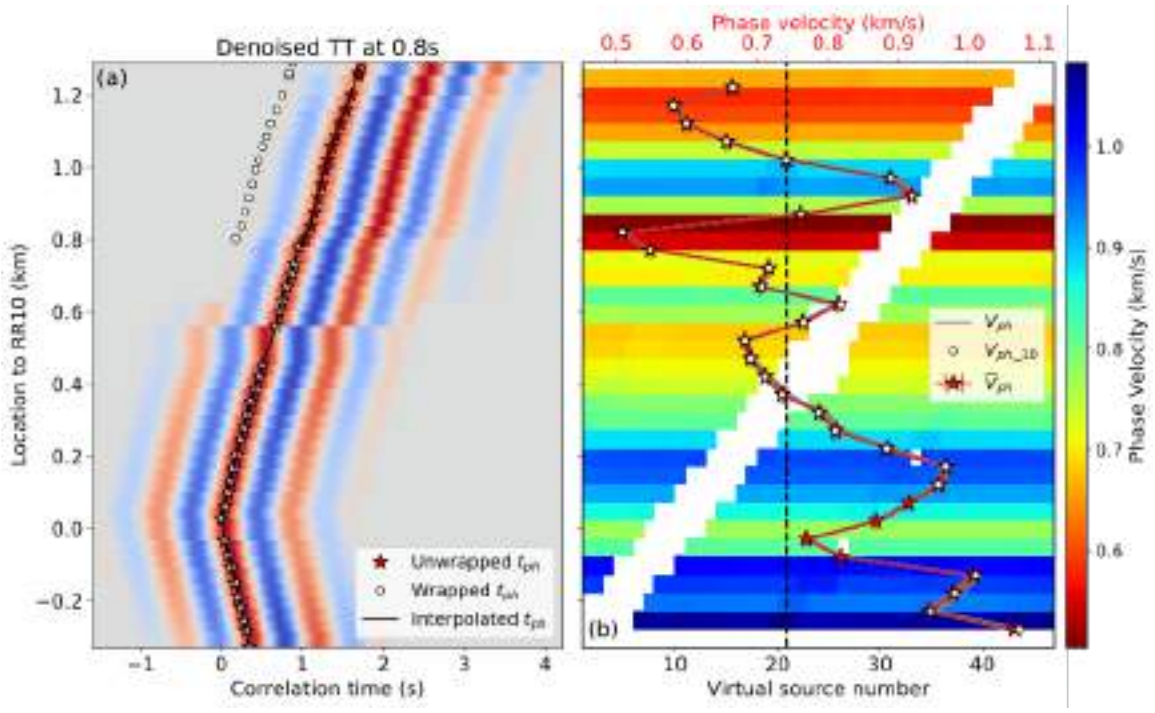

Figure S9. Same as Fig. 5 for denoised data of TT component narrow bandpass filtered at 0.8s.

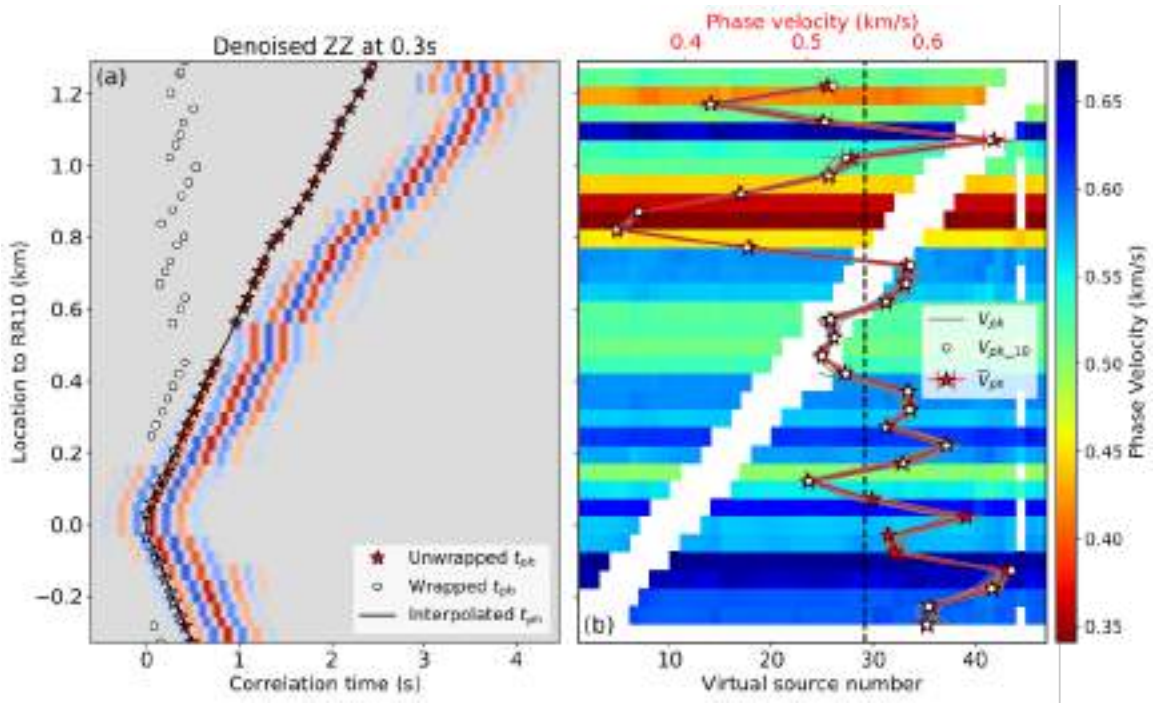

Figure S10. Same as Fig. 5 for denoised data of ZZ component narrow bandpass filtered at 0.3 s.

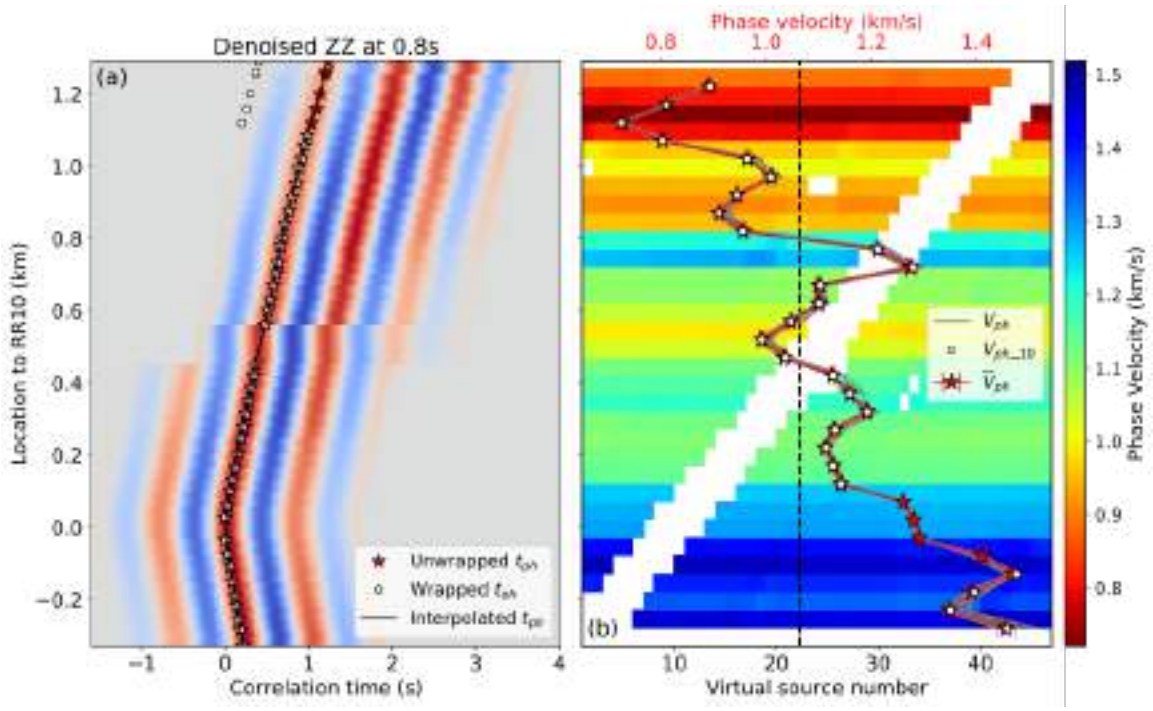

Figure S11. Same as Fig. 5 for denoised data of ZZ component narrow bandpass filtered at 0.8s.

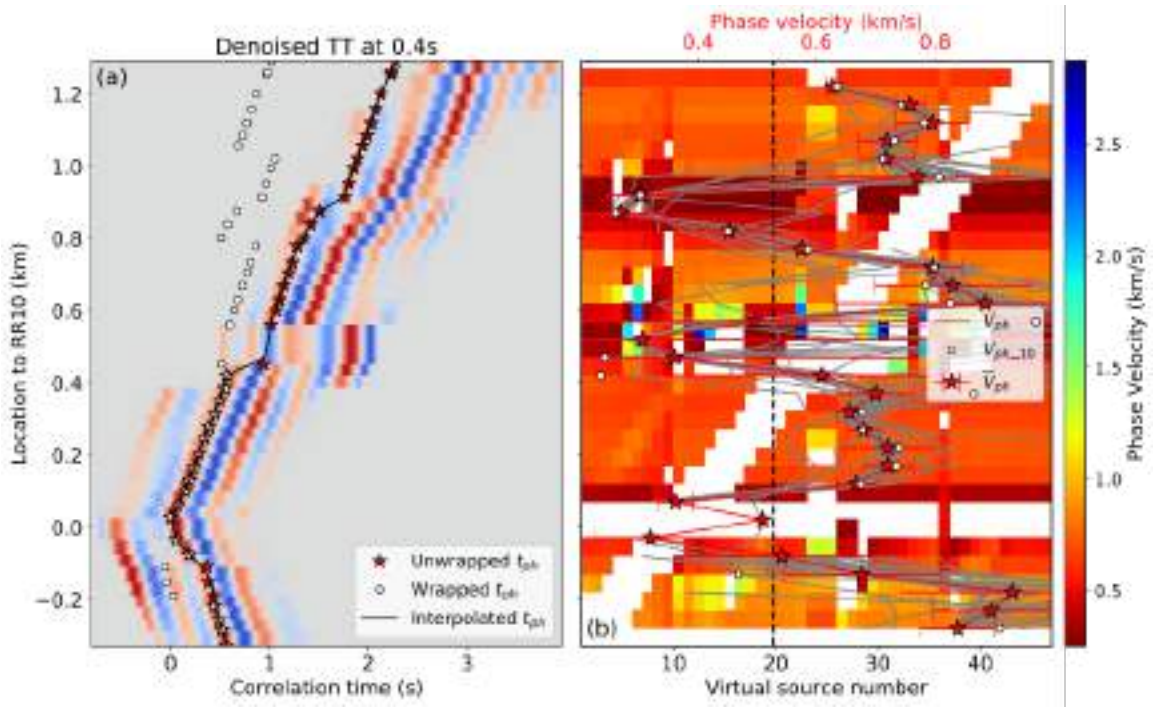

Figure S12. Same as Fig. 5 for denoised data of TT component narrow bandpass filtered at 0.4 s. Denoised waveforms after tapering are less coherent in (a) compared to results at other periods. Phase velocity models inferred from different virtual shot gather (gray curves and colormap) are in general inconsistent and thus yield large uncertainty values.

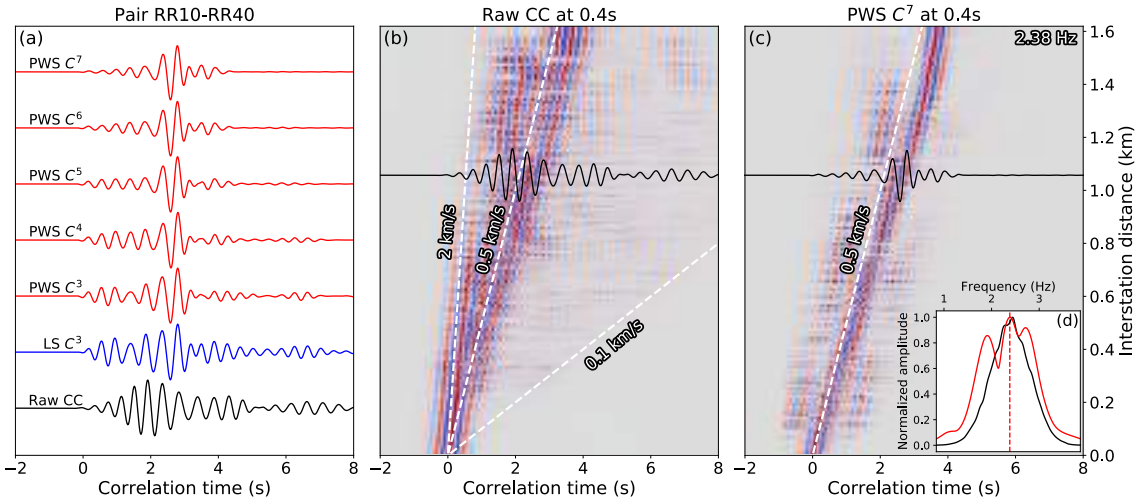

Figure S13. Same as Fig. 3 for the denoising of TT component data narrow bandpass filtered at 0.4 s. Coherent waves that travel at a slightly faster speed with weaker amplitude than the fundamental surface waves are observed in (c), the wavefield after denoising. In addition, the amplitude spectrum after denoising shows 2-3 peaks compared, which is consistent with the observation that there is likely non-negligible higher-mode surface waves with a slightly different dominate frequency in the denoised wavefield.

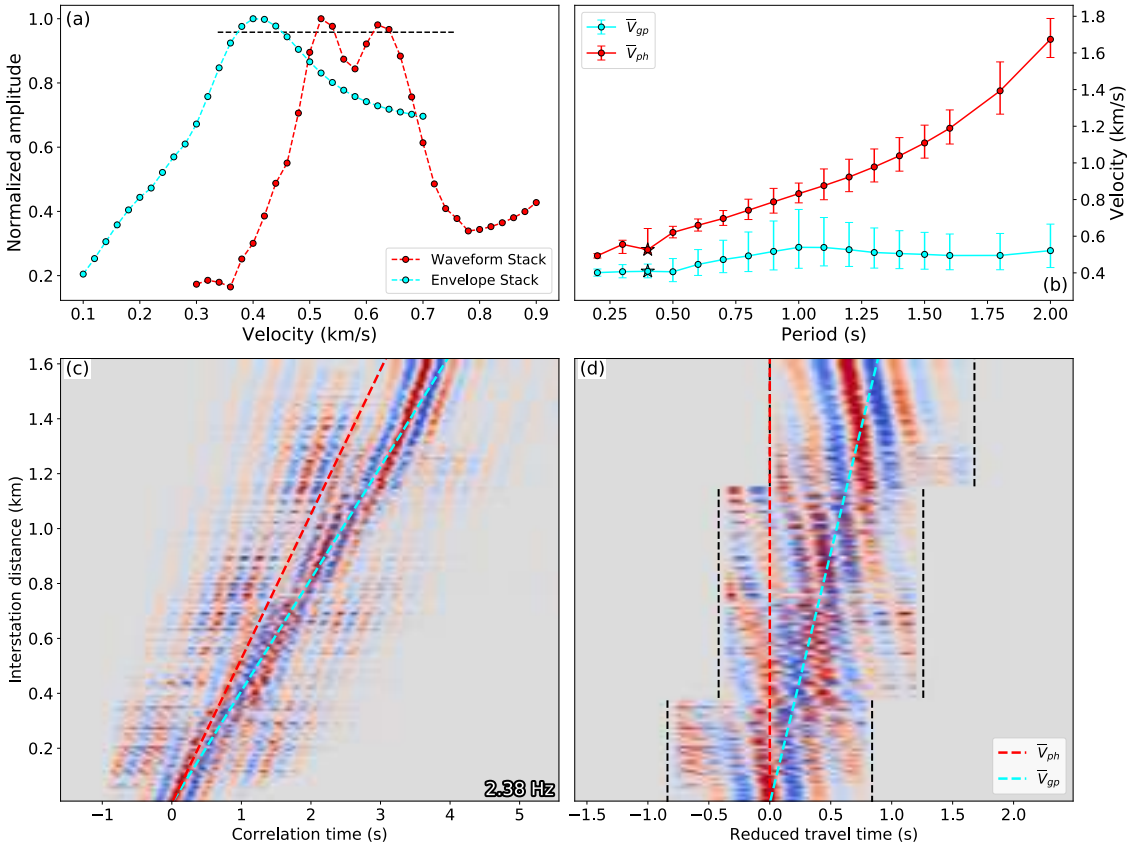

Figure S14. Same as Fig. S5 for the denoised data of TT component narrow bandpass filtered at 0.4 s. Different from Fig. S5, two peaks are found in the grid search curve for array-mean Love wave phase velocity shown in (a), suggesting there are at least two modes of surface waves in the final denoised wavefield shown in (c).

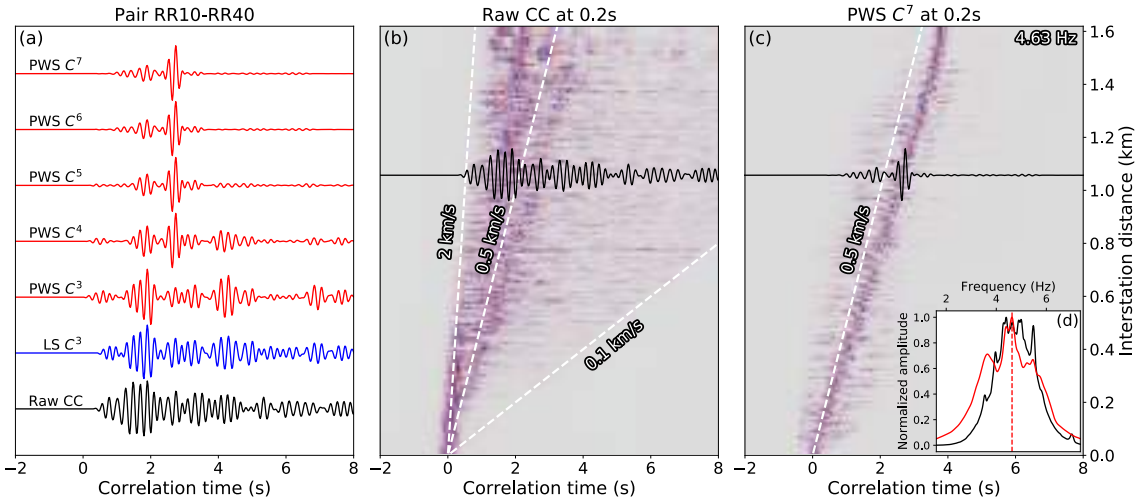

Figure S15. Same as Fig. 4 for the denoising of TT component data narrow bandpass filtered at 0.2 s. Compared to the filtered ANCs in (b), the fundamental mode surface waves are significantly enhanced after the denoising in (c). In addition, similar to Fig. S13, both (c) and (d) may indicate the existence of weak higher mode surface waves in the denoised wavefield at 0.2 s.

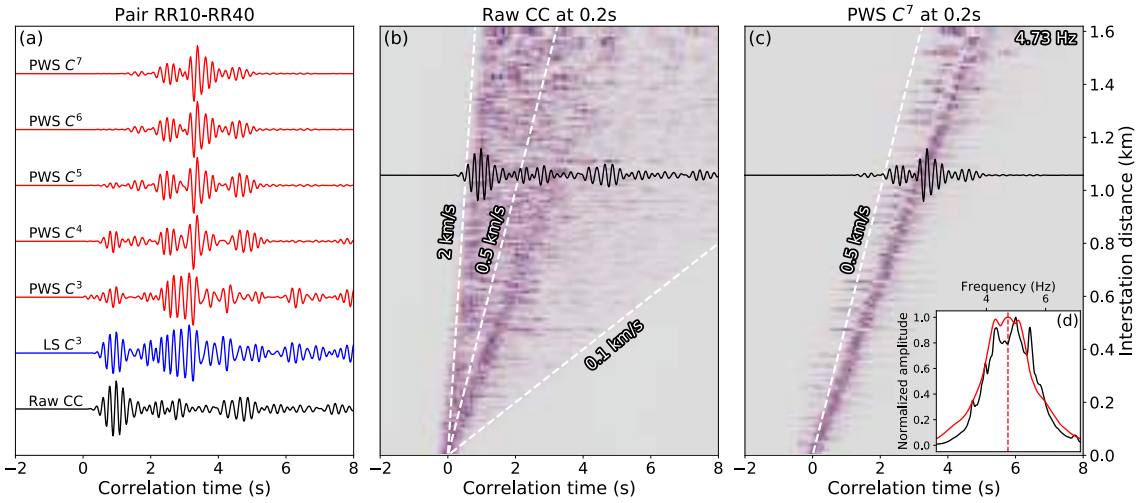

Figure S16. Same as Fig. 4 for the denoising of ZZ component data narrow bandpass filtered at 0.2 s. Fundamental mode surface waves are significantly enhanced after the denoising process from (b) to (c).